Hydrothermal epitaxy growth of self-organized vanadium dioxide 3D structures with metal–insulator transition and THz transmission switch properties

Article *in* CrystEngComm · February 2020

DOI: 10.1039/C9CE01894H

10 authors, including:

Artem Makarevich
Lomonosov Moscow State University
29 PUBLICATIONS **149** CITATIONS
SEE PROFILE

Alexey V. Ivanov
Lomonosov Moscow State University
3 PUBLICATIONS **2** CITATIONS
SEE PROFILE

Andrei Eliseev
Lomonosov Moscow State University
239 PUBLICATIONS **2,255** CITATIONS
SEE PROFILE

Olga Boytsova
Russian Academy of Sciences
44 PUBLICATIONS **179** CITATIONS
SEE PROFILE

CrystEngComm

Accepted Manuscript

This article can be cited before page numbers have been issued, to do this please use: A. M. Makarevich, O. Makarevich, A. Ivanov, D. Sharovarov, A. A. Eliseev, V. Amelichev, O. Boytsova, A. Gorodetsky, M. Navarro-Cia and A. Kaul, *CrystEngComm*, 2020, DOI: 10.1039/C9CE01894H.

ROYAL SOCIETY OF CHEMISTRY

rsc.li/crystengcomm

View Article Online
DOI: 10.1039/C9CE01894H

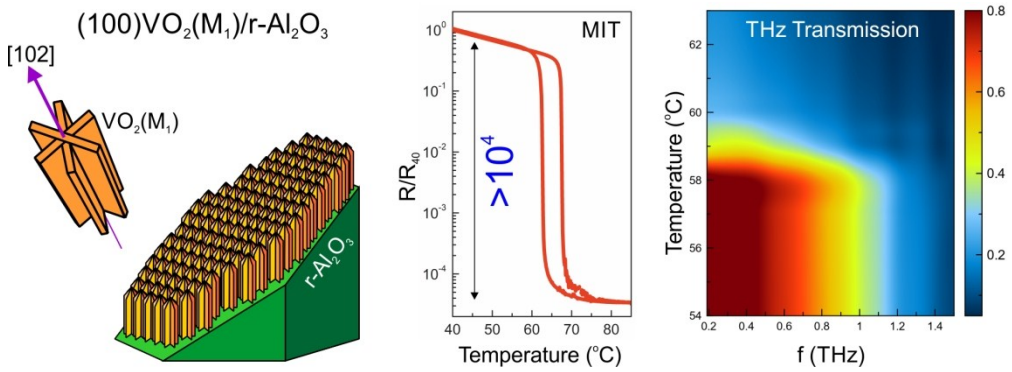

The hydrothermal synthesis of oriented six-pointed VO2(M1) caramboles on r-Al2O3 with large metal-insulator transition and terahertz transmission switch properties.

View Article Online
DOI: 10.1039/C9CE01894H

ARTICLE

Hydrothermal epitaxy growth of self-organized vanadium dioxide 3D structures with metal-insulator transition and THz transmission switch properties

Received 00th January 20xx,
Accepted 00th January 20xx

DOI: 10.1039/x0xx00000x

A. Makarevich[a,d,†], O. Makarevich[a], A. Ivanov[b], D. Sharovarov[b], A. Eliseev[b], V. Amelichev[d], O. Boytsova[a,b,c,§], A. Gorodetsky[e,f], M. Navarro-Cía[f], A. Kaul[a]

The hydrothermal method is the most effective approach for the synthesis of VO_2 metastable polymorphes with unique powder crystallites morphology. In this work, we expanded the capabilities of this method, directing it to the growth of oriented crystallites in self-organized systems on the single crystal substrates. According to our investigations, a large variety of 3D structures of vanadium dioxide can be obtained using one single crystal substrate of r-sapphire by fine tuning of synthesis parameters. The orientation growth of six-pointed vanadium dioxide crystallites fits into the epitaxial growth model describing unit cell relations between the $VO_2(M_1)$ film and r-sapphire substrate. We describe the process of the $VO_2(M_1)$ phase stabilization in the films and the changes of resistivity and terahertz transparency of the films based on the metal-insulator transition (MIT).

1. Introduction

Vanadium (IV) oxide is one of the electron correlated materials which undergoes MIT close to room temperature (68°C) accompanied with a structural transformation between two thermodynamically stable phases: $VO_2(M_1)$ ($P2_1/c$, a=5.75, b=4.54, c=5.38, β=122.64) which is a semiconductor with high resistivity and $VO_2(R)$ ($P4_2/mnm$, a=b=4.55, c=2.86) with metallic properties[1]. The MIT of VO_2 is ultrafast (< 1 ps) and demonstrates the electrical resistance change up to 4 orders of magnitude[2,3]. Due to the capability for modulation of IR, terahertz (THz) and microwave radiation the application of this material opens the opportunities to create fast optical switching devices[4,5], sensors[6,7], thermochromic smart windows[8,9], terahertz[10,11] and photoelectric devices[12] and others[13,14].

Vanadium dioxide epitaxial films on single crystal substrates are most effective for practical issues as they exhibit strong stability to temperature cycling and demonstrate the best MIT characteristics[2,3]. The main difficulty in the synthesis of VO_2 films is the control of V:O ratio which dramatically effects films properties. A number of different physical techniques (magnetron sputtering[15], PLD[16,17], MBE[18]) as well as chemical methods (MOCVD[19], ALD[20], vapor transport method[21]) were used to VO_2 thin films prepare. Wet chemical deposition of VO_2 films can also be realized by the sol-gel technique using the solution of vanadium(V) propoxide, followed by an annealing to reduce V_2O_5 to VO_2[22].

Among the solution methods, the hydrothermal epitaxy method holds a special place due to its important advantages: low cost of reagents and instrumentation, low synthesis temperatures, and a high film growth rate. In the case of epitaxial coatings, the hydrothermal method shows high efficiency in growth of nanorods and dense films, that was demonstrated for ZnO[23,24], TiO_2[25] and $MTiO_3$ (M = Pb[26], Ba[27]). The technique is widely used for the stabilization of phases that are unstable under normal conditions. In particular for vanadium dioxide, several metastable modifications have been obtained in hydrothermal conditions: A, B, D and P[28-32]. These modifications of VO_2 also demonstrate interesting properties[33], for instance $VO_2(B)$, having a layered structure, is a prospective electrode material for lithium and sodium batteries[34,35]. The phases $VO_2(A)$ ($P4_2/ncm$, a=b=8.45, c=7.68) and $VO_2(B)$ (C2/m, a=12.05, b=3.69, c=6.42, β=106.96) have been obtained as epitaxy stabilized films on perovskite-like substrates with close crystallographic parameters[36].

The peculiarity of the hydrothermal approach is also the ability to produce VO_2 powders with a unique crystallites morphology[37,38]. $VO_2(B)$ powders of a star-shape or flower-shape morphology (the later sometimes named as carambola) were obtained by the hydrothermal method for the first time by S. Zhang[39] from commercial V_2O_5 powder and oxalic acid in an aqueous solution, later on it was confirmed in the works[40-42].

The hydrothermal process based on the decomposition of a vanadium (IV) oxalate complex in water solutions at 230°C was

[a] Department of Chemistry, Lomonosov Moscow State University, Moscow, 119991, Russia.
[b] Department of Material Science, Lomonosov Moscow State University, Moscow, 119991, Russia.
[c] Kurnakov Institute of General and Inorganic Chemistry RAS, Moscow, 119991, Russia.
[d] SuperOx, 20/2 Nauchnyi proezd, Moscow, 117246, Russia.
[e] ITMO University, St. Petersburg 197101, Russia
[f] School of Physics and Astronomy, University of Birmingham, B15 2TT, Birmingham, UK.
† makarevich@inorg.chem.msu.ru
§ boytsova@gmail.com

applied to the synthesis of biaxial oriented vanadium dioxide nanonet structures on c-sapphire and (001)TiO_2 substrates[43,44]. Such a strategy allowed obtaining 3D structures of interconnecting VO_2 nanorods with the morphology depending on the symmetry of substrate surfaces. Therefore the possibility of hydrothermal epitaxial growth of oriented VO_2 structures on single-crystal surfaces opens new prospect for designing VO_2 – based materials for practical applications.

In this work, we describe the hydrothermal epitaxy method for the preparation of biaxially textured VO_2 structures on r-sapphire substrates at the temperatures less than 200°C. We show that the films of different VO_2 polymorphs can be obtained of several morphological types using one type of substrate surface by changing parameters of hydrothermal synthesis (temperature, time and solution concentration). The paper describes the method of M_1-phase stabilization, as well as the results of the resistivity and Terahertz transmittance measurements of the films obtained.

2. Experimental

2.1 Starting materials and synthesis

The precursor solution was prepared by mixing ammonium metavanadate (0.01 mol) and oxalic acid (0.02 mol) in 100 ml of distillate water under stirring and heating (~60°C) during 6 hours resulting in a deep blue solution.

For hydrothermal synthesis the initial solution was diluted with distillate water to achieve the desired concentration (0.005 or 0.02 M) and was placed into the Teflon liner with one-side polished single crystal r-cut sapphire substrates (r-Al_2O_3) of 15x10 mm in size. Then the liner was placed into the stainless steel autoclave and heated to 195 or 200°C for 4-6 h, followed by cooling to the room temperature during 1 hour. The resulting black precipitate separated by centrifugation and the films on the substrates were washed with distilled water and ethanol and dried with air. The detailed parameters of hydrothermal synthesis are given in Table 1.

Annealing of the as-prepared films was carried out in a quartz reactor in an argon flow of 5 l/h at the total pressure of 3 mbar. The time and temperature of anneal setup were varied in the range of 30-90 min and 400-600°C, respectively.

2.2. Characterization

X-ray diffraction (XRD) analyses of powders were performed on a Rigaku SmartLab in Bragg-Brentano geometry with graphite monochromator in the diffracted beam. XRD analysis of films was conducted on a Rigaku SmartLab in parallel beam geometry with a Ge(220)×2 monochromator in the primary beam (λ=1.54046 Å). The diffraction in 2θ scanning mode was performed with 0.02° steps at a speed of 5°/min. Phase identification was performed using the JCPDS database.

IR spectroscopy of complexes was registered using FTIR SpectrumOne by PerkinElmer in the mode of disturbed total internal reflection, in the region of 400-4000 cm^{-1}, with a resolution of 0.5 cm^{-1}.

Differential thermal (DTA) and thermogravimetric (TGA) analysis of the samples was performed on STA 409 PC Luxx (Netzsch). Measurements were carried out in air atmosphere in the temperature range from room to 700°C with heating rates of 5 and 10°C/min. A quadrupole mass spectrometer with heating of the capillary system of the inlet Aeolos QMS 403 C (Netzsch) was used to study the exhaust gases.

The morphology of the powders and films was characterized by scanning electron microscopy using FEI Helios Nano Lab 600 DualBeam FESEM at a 5 keV acceleration voltage and current 86 pA in the through-the-lens (TLD) regime.

Raman spectra were recorded using Renishaw InVia spectrometer/microscope with 514 nm laser excitation and 2400 l/mm grating at room temperature. To avoid the heating of the samples under laser irradiation the laser (20 mW power) was defocused to ~20 μm spot.

The temperature dependences of resistance were measured by the four-contact method with a home-made setup, using clamping copper contacts. The measurements were carried out in the temperature range of 35-90°C.

Terahertz (THz) spectroscopic characterization was performed with Menlo TERA K15 THz time-domain spectrometer (TDS). The temperature upon characterization was maintained by Thorlabs TC-200 temperature controller and Thorlabs HT-19R metal-ceramic heater and monitored with Thorlabs TH100PT temperature detector. Spectroscopic measurements allowed of THz transmission through the sample were performed in the range of 0.1-2.0 THz, and the temperature was maintained with 0.1°C precision.

3. Results and discussion

3.1 Precursor analysis

From the literature data it is known[45] that the reaction of ammonium metavanadate with oxalic acid proceeds with the formation of an oxalate complex of vanadyl:

$2NH_4VO_3 + 4H_2C_2O_4 = (NH_4)_2[(VO)_2(C_2O_4)_3(H_2O)_2] + 2H_2O + 2CO_2$ (1).

Table 1. The parameters of hydrothermal synthesis of the described samples.

sample №	C, M	V_0, ml	V/V_0, %	T, °C	t, h
1	0.005	10	90	200	4
2	0.02	10	90	195	6
3	0.02	25	90	200	6
4	0.02	25	90	195	6

View Article Online
DOI: 10.1039/C9CE01894H

ARTICLE

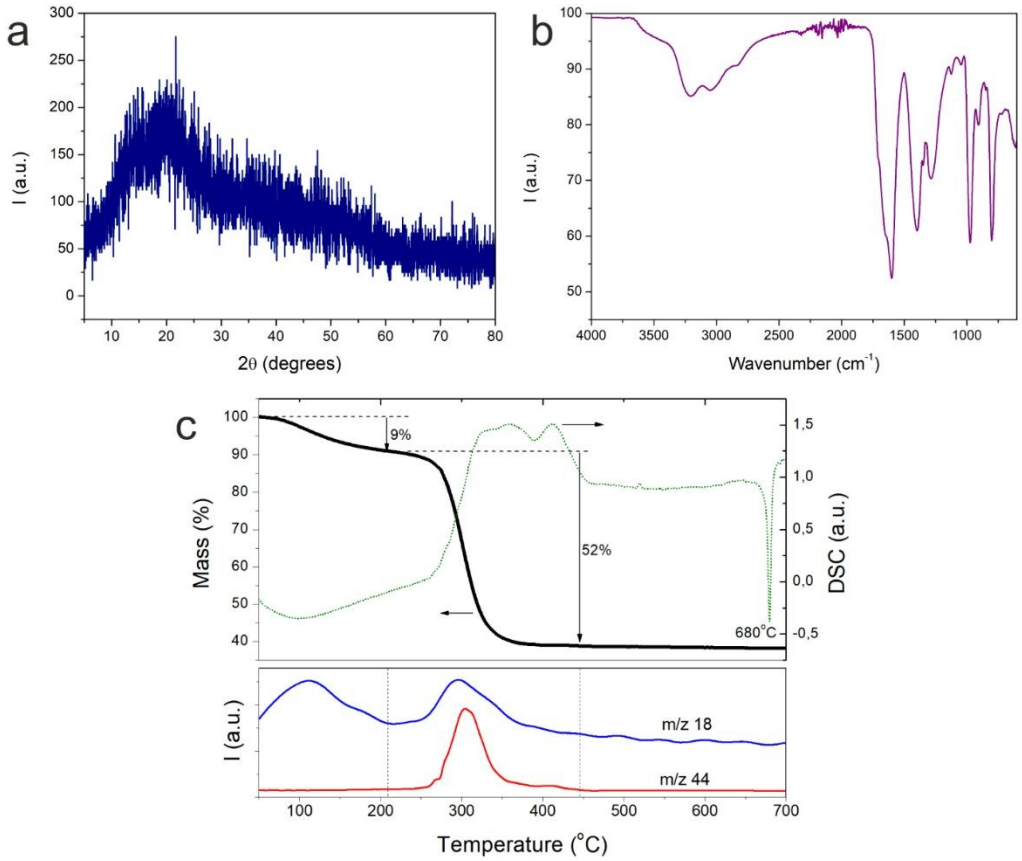

Fig. 1. Characterization of solid precursor $(NH_4)_2[(VO)_2(C_2O_4)_3(H_2O)_2]$: XRD (a), IR spectrum (b) and TGA-MS (c).

We confirmed the formation of this intermediate substance using the IR-spectroscopy and TG-MS method. The blue solid powder was separated from the solution by evaporation on air. According to the XRD pattern the product is amorphous with no reflections of initial reagents (Fig. 1a). The IR spectrum of the obtained powder (Fig. 1b) contains all the absorption bands corresponding to the proposed composition: 3050-3200 cm^{-1} ν(OH), 1594 cm^{-1} $\nu_{as}(COO^-)$, 1398 cm^{-1} $\nu_s(COO^-)$ + $\delta(NH_4^+)$, 1287 cm^{-1} ν(C-O), 974 cm^{-1} ν(V=O), 804 cm^{-1} δ(V-O).

According to the thermal analysis of powders with mass-spectrometric determination of the exhaust gases there are two stages of precursor decomposition. At the first stage (up to 260°C) the hydrate water is cleaved (m/z = 18), the found mass loss is 9% (calculated 8%). At the second stage (up to 260-400°C) the product is burned with the release of water (m/z = 18) and carbon dioxide (m/z = 44) that corresponds to exothermic effect on the DSC curve. The analysis was performed in air so the combustion product is V_2O_5, which was confirmed by a sharp endothermic peak on the DSC curve at 680°C, corresponding to its melting. The found mass loss for this stage is 52% (calculated 53%).

3.2 Synthesis of polycrystalline products

According to the thermal analysis, the vanadyl oxalate complex is stable up to 250°C. The mechanism of the vanadium dioxide phase formation from vanadyl oxalate complexes under hydrothermal conditions at temperatures less 200°C remains questionable. The decomposition of an oxalate complex to VO_2 can be written as the following presumptive reaction:

$(NH_4)_2[(VO)_2(C_2O_4)_3(H_2O)_2] = 2VO_2\downarrow + 3CO + 3CO_2 + 2NH_3 + 3H_2O$ (2).

According to SEM (Fig. 2a) the hydrothermal synthesis from the solution of the vanadyl oxalate complex results in the volume precipitation of a black powder consisting of spherical particles with a diameter of about 2 μm. The powder particles have a highly developed surface composed by six-pointed carambola-

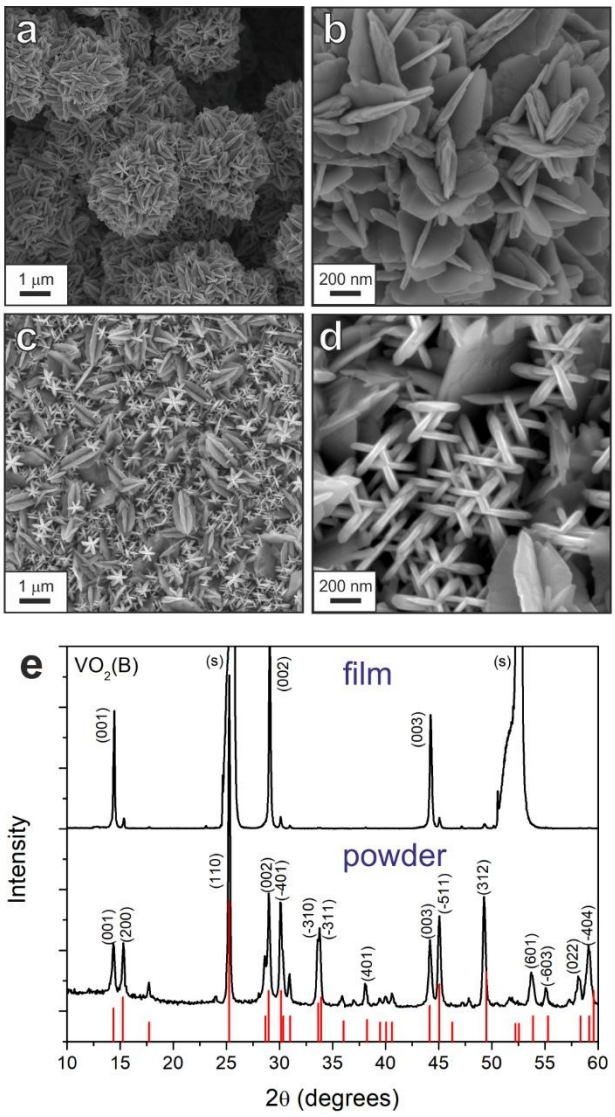

Fig. 2. Analysis of the products obtained after hydrothermal synthesis from solution 0.1 M: SEM of powder (a, b) and polycrystalline film (c, d), XRD (e) with card of VO_2(B) (JCPDS 31-1438).

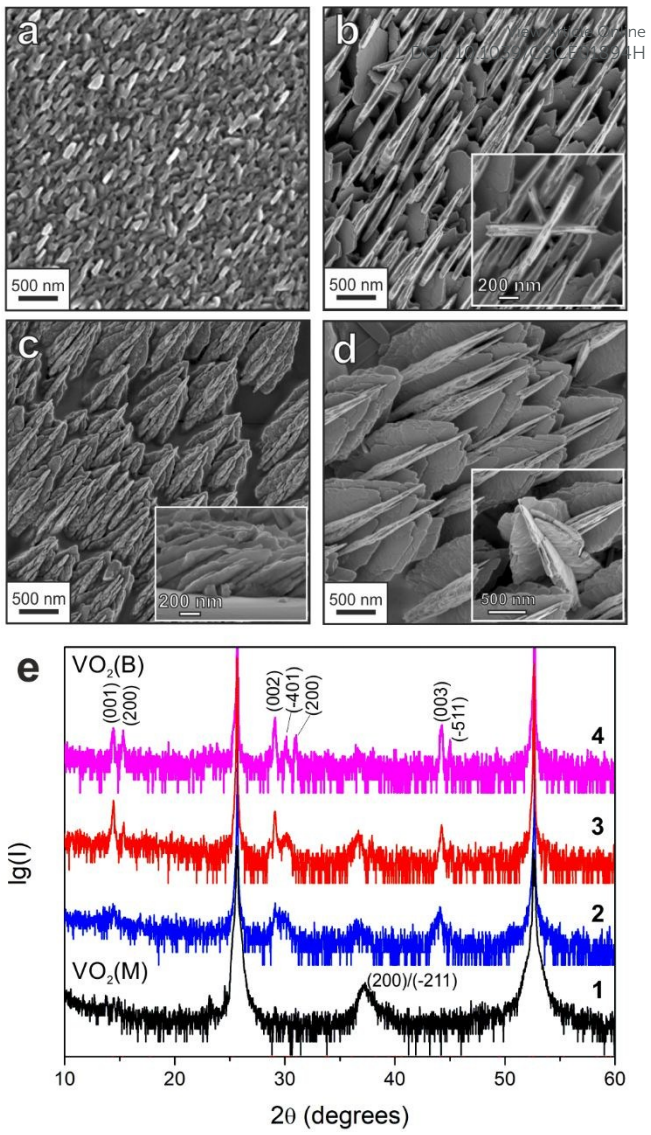

Fig. 3. Characterisation of samples 1-4 by SEM (a-d) and XRD (e). For images b and d the self assembly defects are shown. The hkl-indexes for reflexes of $VO_2(M_1)$ and VO_2(B) phases are presented in cases of samples 1 and 4, respectively.

like crystallites: ~200 nm size plates arranged to each other at an angle close to 60° (Fig. 2b). The XRD data (Fig. 2e) confirm the formation of the monoclinic VO_2(B) phase (JCPDS 31-1438).

The single crystal sapphire substrates with the cutting r-plane (10-12) were also used as seeding substrates to obtain the film samples from hydrothermal conditions. A dense black film with the morphology similar to the powder sample (Fig. 2c, d) was formed on the substrate at the same conditions of growth (concentration 0.1 M, filling degree 90%). However, the XRD pattern (Fig. 2e) shows that the film has a distinct texture of (001)VO_2(B). Since the film looks polycrystalline on the SEM images, it can be concluded that the inner layer adjacent to the surface of the sapphire substrate is oriented.

3.3 The growth of oriented structures

There is a supersaturation of the solution by the decomposition products of precursor molecules under the conditions of hydrothermal synthesis. As a result the nucleation and growth of new phases crystallites occur both by the homogeneous mechanism in the volume of the solution and by the heterogeneous mechanism on the walls of the liner or on the surface of the substrate. The formation of vanadium dioxide phase crystallites on the coherent surface of the r-Al_2O_3 substrate is significantly more energy-efficient than the homogeneous mechanism in the solution volume, because it reduces the energy barrier of the nucleation stage. Therefore, it is possible to choose conditions in which a small value of concentration supersaturation will lead to the formation of the VO_2 phase mostly on the substrate surface.

We varied some conditions of hydrothermal synthesis in order to reduce the rate of formation of the vanadium dioxide phase particles in the solution volume and to realize the oriented

View Article Online
DOI: 10.1039/C9CE01894H

growth of vanadium dioxide phase crystallites on the r-sapphire surface by the mechanism of epitaxial growth. To affect the growth kinetics we decreased the concentration of the solution and the temperature but increased the synthesis time to grow the density of vanadium dioxide crystallite packing over the entire substrate area.

The proposed methods of controlling the kinetics of the process made it possible to realize the oriented growth of VO_2 on the surface of the substrates. This paper presents the results for 4 samples, the conditions for their obtaining are shown in table 1 (see Experimental).

It should be noted, despite the slight differences in the synthesis conditions, the morphologies of the obtained samples vary greatly. Thus, the use of the lowest concentration 0.005 M led to the formation of an ordered porous film consisting of anisotropic particles of 30x200 nm in size (Fig. 3a). SEM image shows that the formation of biaxially textured structures occurred on the surface of the substrates, indicating epitaxial growth. The increase of the concentration of up to 0.02 M led to the formation of 3D structured with self-ordered VO_2(B) phase flat crystallites (Fig. 3b). A similar microstructure of a VO_2 film was obtained by hydrothermal synthesis at 230°C for 4 hours from V_2O_5 and oxalic acid[43].

The hydrothermal process takes place in a closed volume containing a limited quantity of reagents, so an increase in the volume of the liner leads to a slower decrease in the concentration of the solution over time (if a heterogeneous mechanism of film formation is carried out). Sample 3 and 4 were obtained in Teflon liner at a volume of 25 ml, which led to a significant increase in the size of crystallites and the total film thickness (about 2 times). Crystallites have a well-articulated carombola-shaped structure, and each carombola inclined to the substrate plane by 32.5° (Fig. 3c).

Even as a small difference in temperature as 5°C led to a significant change in the morphology of the coatings. The film obtained at 200°C (sample 3) consists of crystallites of a smaller size, however, the faces of the carambolas are thicker than in the case of sample 4, and the carambolas are more evenly located on the substrate area.

Due to the high texture, the XRD patterns of the samples (Fig. 3e) contain a limited number of reflexes, which makes it difficult to identify the phases. The low synthesis temperature creates an additional difficulty, therefore there is no certainty that all phases give distinguishable reflexes on the XRD patterns. It can be argued that there is an M_1-phase in the composition of the films, because of the presence of the low-intensity reflex about 37° which corresponds to the plane (200)/(-211). This reflex is most expressed in the case of sample 1, herewith the reflexes of B-phase are absent. If we move from sample 2 to sample 4, the intensity of B-phase reflexes increases, and the reflex of M_1-phase becomes barely distinguishable. Based on this, we can assume that the M_1-phase is concentrated near the substrate surface and further thickening of the film takes place only due to the B-phase.

For sample 2 with a low intensive XRD pattern the formation of the metastable VO_2(B) phase was proved by Raman spectroscopy

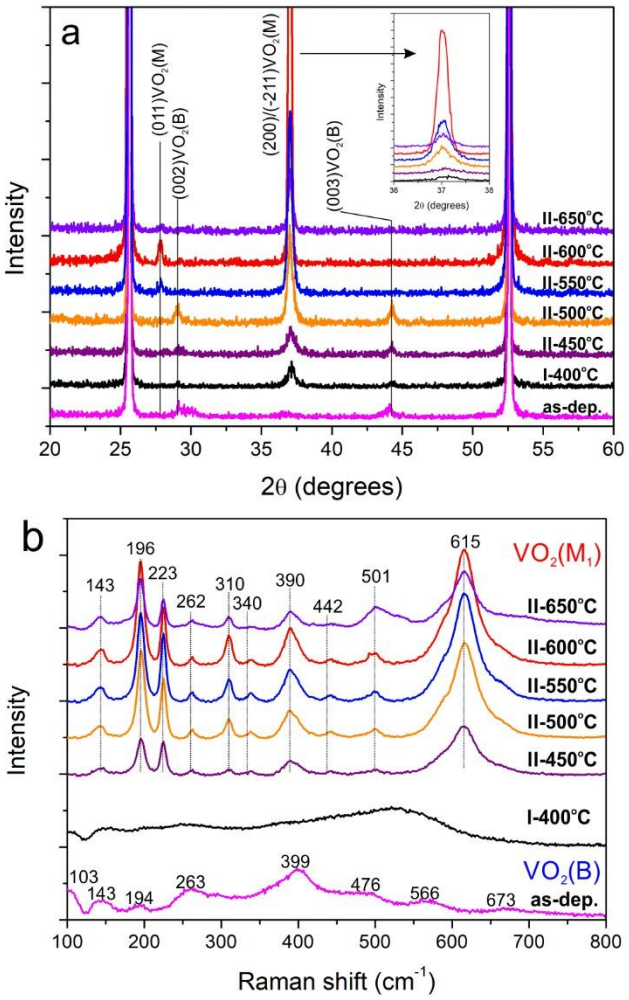

Fig. 4. Characterization of sample 2 after two-step annealing (showed number of final step and annealing temperature): XRD (a) and Raman spectroscopy (b).

(Fig. 4b). The spectrum clearly illustrates Raman lines located at 103, 194, 263, 399, 476 and 673 cm^{-1} typical for the vibration modes of VO_2(B)[46]. Additional bands at 143 and 566 cm^{-1} have not been earlier described for the vanadium oxide B phase. As it is resumed in the recent review[46], the Raman spectra of VO_2 metastable phases are poorly described in the literature and it is difficult to detect the presence of additional phases, their consideration remains in question. According to HRTEM, TEM and related SAED of as-deposited sample weak crystallinity was determined due to low quality of EM images. The assumed relation between film and substrate may be described as VO_2(B) $(-202)_f \perp (01\text{-}12)_s$ (ISE, Figure S1)

3.4 Annealing of the samples

Annealing of the vanadium dioxide films is a frequently used procedure to improve their electrical properties. First of all, this is due to the need to consolidate the grains and to increase the size of the crystallites of the M_1-phase, as secondary phases and defects at the grain boundaries dramatically decrease the performance of the MIT. In our case annealing is also necessary

because of the phase VO_2(B), which is more stable under hydrothermal conditions, should be transformed into the M_1-phase possessing of MIT. We worked out the conditions of temperature treatment on the films obtained by analogy with sample 2. The variation of the temperature, time and atmosphere of annealing showed that the best result can

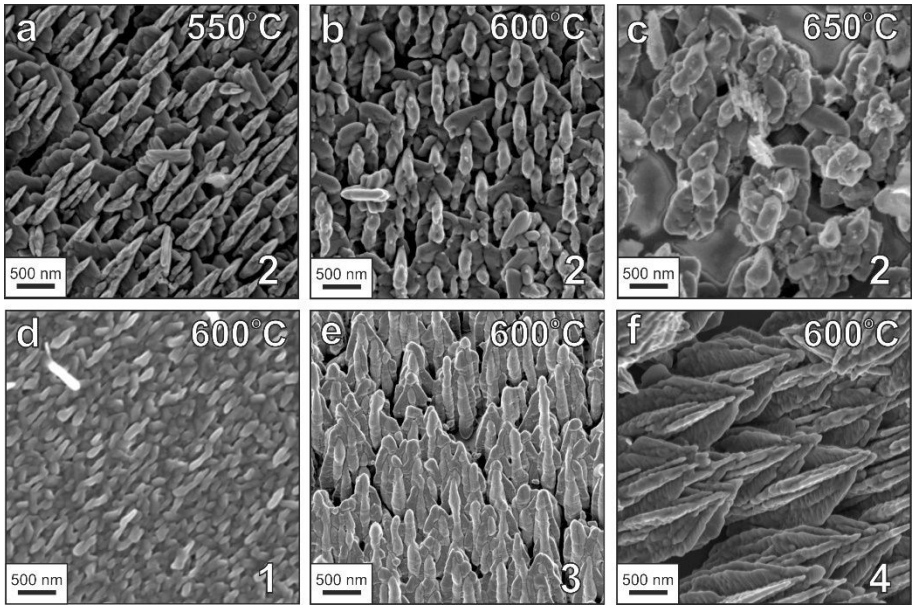

Fig. 5. The SEM images of sample 2 annealed at temperatures 550-650 (a-c) and samples 1, 3 and 4 annealed at 600°C (d, e and f, respectively).

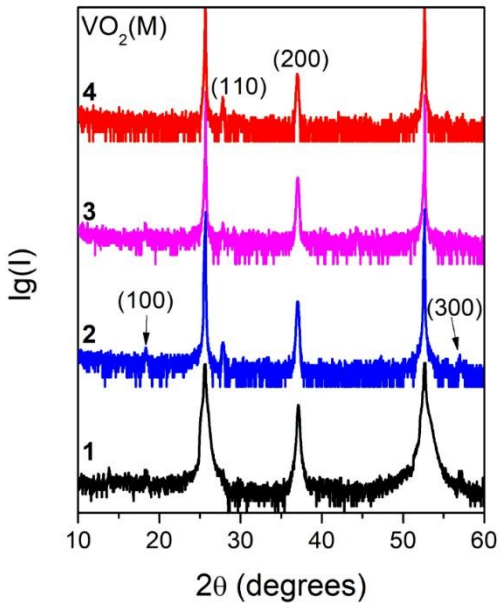

Fig. 6. The XRD analysis of samples 1-4 after annealing at 600°C.

be obtained for the samples annealed in two-stage procedure: at 400 °C and then at 600 °C in an argon flow at the total pressure of 3 mbar. This method avoids the oxidation of crystallites at the stage of their transformation into the M_1-phase, while maintaining the biaxial texture of the crystallites.

Fig. 4a shows the XRD patterns of the sample obtained after the first stage at 400°C for 30 min, it is seen that the ratio of reflexes in B- and M_1-phases was changed, the intensity of the reflex (200)$VO_2(M_1)$ was increased significantly. As the temperature of the second annealing stage increases, the intensity of the $VO_2(M_1)$ phase signals grows. The VO_2(B) phase reflexes disappear completely only at 600 °C, which shows the kinetic difficulty of converting the B- into the M_1-phase. The results obtained are consistent with the literature data[47]. Similar results were shown by Y. Luo[48], who found the transition of the VO_2(B) to $VO_2(M_1)$ phase to proceed in the range 400-550°. In our samples the intensity of the reflex (200)/(-211) begins to decrease at 650°C, indicating the destruction of the film as a result of oxidation and partial peritectic melting[19]. The formation of $VO_2(M_1)$ phase in the temperature range of 450-650°C was also proven by Raman spectroscopy (Fig. 4b) showing all vibration modes of $VO_2(M_1)$ in spectra[46]. One can suggest that the bands of VO_2(B) are poorly visible in the presence of M_1-phase, due to possible localization of the B-phase in the film volume. The degradation of the M_1-phase after annealing at 650°C led to decreasing the bands intensity and their broadening especially in the case of 615 cm^{-1}.

Fig. 5(a-c) shows the SEM images of films after the first stage of annealing at 400 °C and after the second stage at 600°C and 650°C. Its demonstrates that annealing at 400°C does not change the structure of crystallites, at 600°C their partial melting and

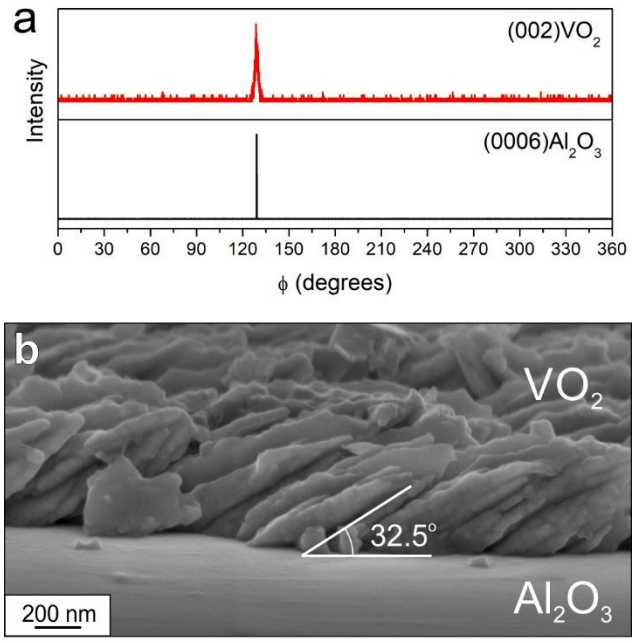

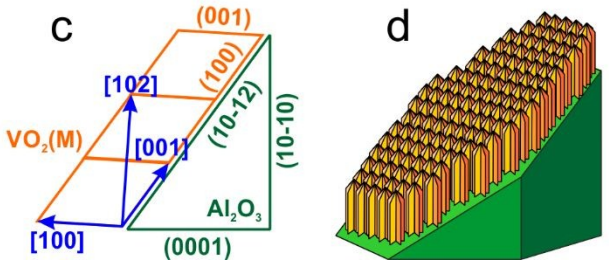

Fig. 7. The analysis of $VO_2(M_1)$ carambols orientation growth on r-Al_2O_3 (sample 3): (a) the ϕ-scanning analysis showed the in plane directions of film crystallites; (b) the cross-section image of the film demonstrated the slope of the carambol growth relative to the surface of r-sapphire; (c) the epitaxial relations between film and substrate unit cells; (d) the model of $VO_2(M_1)$ film growth on r-sapphire as a result of the hydrothermal epitaxy approach.

sintering occurs, and at 650°C the carambola-like structure of the film is destroyed as a result of strong melting.

Two-stage annealing with a temperature of 600°C in the second stage was effective for samples 3 and 4. In both case, the result was a significant increase of the $VO_2(M_1)$ reflex (200)/(-211)VO_2 and the disappearance of B-phase reflexes (Fig. 6).

3.5 Orientation of $VO_2(M_1)$/r-Al_2O_3 films

Fig. 7a shows the results of ϕ-scanning for the reflex (002)$VO_2(M_1)$ for the sample obtained at 600°C, it confirms the biaxial texture of the film obtained and together with the results of 2θ-scanning (Fig. 6) make it possible to write epitaxial relations between the film and the substrate: (100)VO_2||(10-12)Al_2O_3, [010]VO_2||[01-10]Al_2O_3. The epitaxial relations are the same as in case of VO_2 films grown on the r-sapphire substrates by MOCD[19] or PLD[16] techniques.

The image of sample 3 cross-section showed the slope of the carambolas growth relative the r-sapphire surface (Fig. 7b). The angle between VO_2 crystallite growth axis and substrate r- plane is about 32.5 degrees. According to scheme of epitaxial

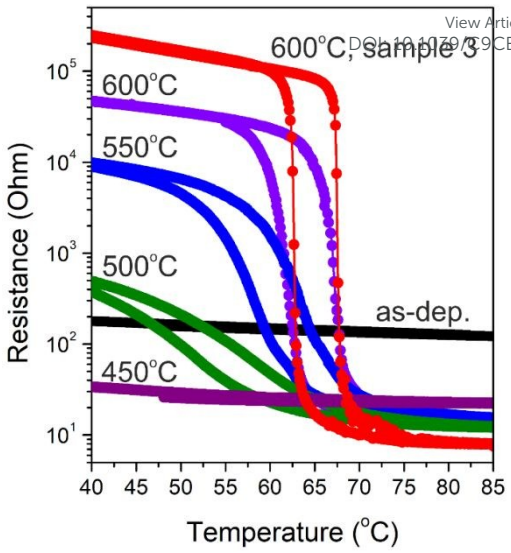

Fig. 8. The electrical properties of samples 2 annealed at different temperatures on the second stage. For comparison the data for sample 3 annealed at 600°C are presented.

relations between $VO_2(M_1)$ film and sapphire substrate (Fig. 9c) the growth of carambolas take place along axis [102]. The TEM image of the cross-section sample and related SAED patterns clearly show evidence of epitaxial relation between substrate and $VO_2(M)$ (ISE, Figure S2). These data are in agreement with the models of formation of six-pointed $VO_2(M_1)$ structures presented in the literature[49,50]. It is interesting, that according to our model in case of c-cut sapphire the growth of hexagonal structures will be orthogonal to substrate surface, that is very close to the result of work[43]. Thus the general approach to the design of VO_2 hexagonal column self-assemble growth is based on determination of [102] axis direction as a result of epitaxial relations between the substrate and $VO_2(M_1)$ unit cell.

3.6 Electrical properties

The effect of the second stage-annealing temperature on resistive MIT-curves was analysed for sample 2 (Fig. 8). It should be noted that the annealing at low temperature significantly reduces the resistance of the film that may be associated with the oxidation of grain boundaries and the appearance of impurity of VO_{2+x} phases with a metal type of conductivity. A further increase in the annealing temperature leads to the increase of $VO_2(M_1)$ grains number (this is consistent with the XRD data), and to the appearance of percolative chains via this grains. This increases the resistance of the films in the low-temperature region and reduces resistance at high temperatures. As a result, the increase of the second stage-temperature of annealing to 600°C makes the MIT sharper and magnifies its amplitude. Samples 1 and 4 annealed at 600°C exhibited the MIT characteristics closed to sample 2 (ISE, Figure S3). The best parameters were shown by sample 3, the transition amplitude at 65°C was about 4 orders of magnitude. The growth of the film thickness and the density of substrate coverage with carambola-like needles lead to an improvement of the MIT characteristics.

3.7 Optoelectronic properties in the THz range

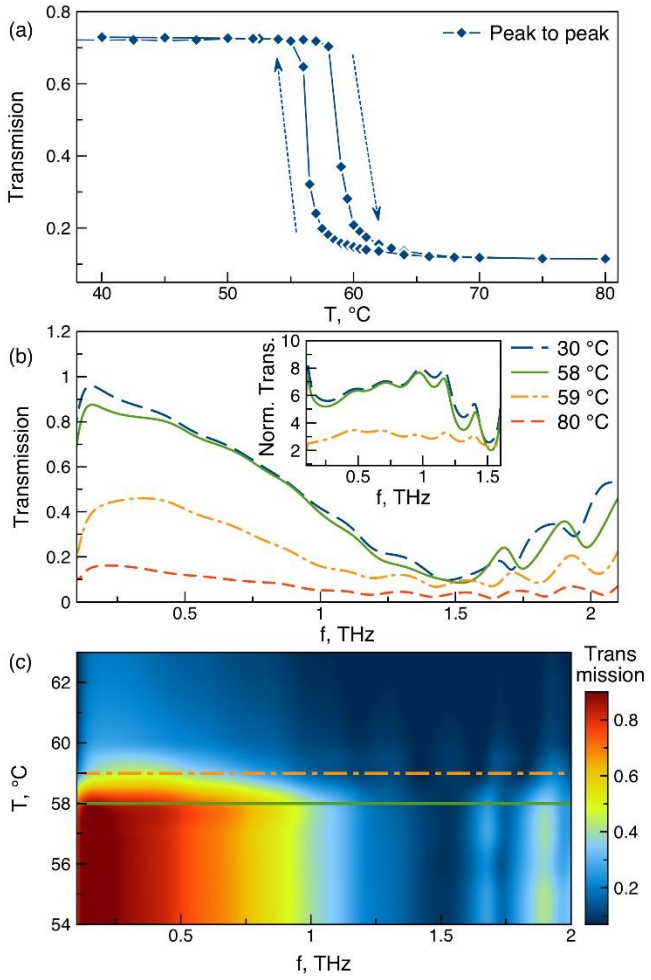

Fig. 9. THz TDS characterization of sample 3 annealed at 600 °C: (a) normalized peak-to-peak THz amplitude dependence on sample temperature, arrows show the direction of the temperature change, (b) amplitude THz transmission spectra at different temperatures, and (c) full temperature dependence of THz transmission spectrum. Cross sections, corresponding to the curves shown in (b) are marked with respective colors. Inset in (b) shows the change in sample transmission with respect to the transmission at 80°C.

The temperature dependence of sample transmission in the range of 0.1-2.0 THz of sample 3 is shown in Fig. 9. To analyse the transmission of the thin film, spectroscopic data obtained for the sample were normalized to the transmission of the substrate. The temperature was varied from ambient (~24 °C) towards 80°C and then in the reverse direction. The observed change in transmission (Fig. 9a) shows the behavior similar to the resistance trend (Fig. 8a) and reveals a sharp 7-fold change between 58° and 60°C. We note that this is an amplitude change, corresponding to the 50-fold change in THz intensity transmission. The transition is observed at lower temperatures if compared to the resistive transition occurring at higher (around 65 °C) temperature values, associated with the percolation model of MIT[19]. From Fig. 9b, it can be seen that thin film sample reveals a spectrally uneven transmission in the THz range that has a broad dip around ~1.5 THz and demonstrates a rather flat 6 to 8 – fold amplitude transmission switch across the broad spectrum between 0.1 and 1.2 THz (inset of Fig. 9b), corresponding to the 35-60 – fold change in transmitted THz intensity. The full map of THz transmission spectrum dependence on temperature shown in Fig. 9c, features some spectral irregularities upon transition around 1 THz.

4. Conclusion

In this work, we showed the feasibility of the hydrothermal epitaxy method for the preparation of biaxially textured VO_2(B) structures on r-sapphire substrates at temperatures less than 200°C from the solutions of a vanadyl oxalate complex precursor. The morphology of crystallites forming the films is highly sensitive to the process parameters affecting growth kinetics: temperature, time and solution concentration. The VO_2(B) phase can be transformed into the $VO_2(M_1)$ phase with a metal-insulator transition (3-4 orders of resistance change) through a two-step annealing process in Ar atmosphere at 400°C and then 600°C while preserving the carambola-like morphology. We summarize that the oriented growth of hexagonal vanadium dioxide crystallites is along [102] axis of $VO_2(M_1)$ and can be predicted according to the epitaxial relations between $VO_2(M_1)$ and substrate surface unit cells. The observed significant reversible change of the transmission in the broad THz range shows a great potential of these epitaxial hydrothermal-derived films for application in tunable THz devices.

Conflicts of interest

There are no conflicts to declare.

Acknowledgements

The work was funded by RFBR according to the research project № 18-03-00858. O.B. thanks the Russian Science Foundation for funding high resolution SEM experiments in the frames of grant № 18-73-10212. The SEM studies were performed using the equipment of the JRC PMR IGIC RAS. The analysis of THz properties was supported in part by the EPSRC (Grant No. EP/S018395/1). M. N.-C. acknowledges support from the Royal Society (Grant No. RSG/R1/180040), and the University of Birmingham (Birmingham Fellowship). A.G. thanks MagicPlot LLC for providing a free copy of MagicPlotPro software.

References

1 F. J. Morin, *Phys. Rev. Lett.*, 1959, **3**, 34.
2 M. Brahlek, L. Zhang, J. Lapano and H.-T. Zhang, *MRS Communic.*, 2017, **7**, 27.
3 Z. Yang, C. Ko, and S. Ramanathan, *Annu. Rev. Mater. Res.*, 2011, **41**, 337.
4 Y. Zhou, X. Chen, C. Ko, Z. Yang, C. Mouli and S. Ramanathan, *IEEE Electron Device Lett.*, 2013, **34**, 220.
5 C.Z. Wu, F. Feng, and Y. Xie, *Chem. Soc. Rev.*, 2013, **42**, 5157.

6 A. Simo, B. Mwakikunga, B. T. Sone, B. Julies, R. Madjoe and M. Maaza, *Int. J. Hydrogen. Energ.,* 2014, **39**, 8147.
7 A. Holsteen, I.S. Kim and L.J. Lauhon, *Nano Lett.,* 2014, **14**, 1898.
8 S. Chen, L. Dai, J. Liu, Y. Gao, X. Liu, Z. Chen, J. Zhou, C. Cao, P. Han, H. Luo and M. Kanahira, *Phys. Chem. Chem. Phys*., 2013, **15**, 17537.
9 C. Liu, N. Wang and Y. Long, *Appl. Surf. Sci*., 2013, **283**, 222.
10 X. Wu, Z. Wu, C. Ji, H. Zhang, Y. Su, Z. Huang, J. Gou, X. Wei, J. Wang and Y. Jiang, *ACS Appl. Mater. Interfaces,* 2016, **8**, 11842.
11 Y.Y. Luo, F.H. Su, S.S. Pan, S.C. Xu, C. Zhang, J. Pan, J.M. Dai, P. Li and G.H. Li, *J. Alloy. Comp.,* 2016, **655**, 442.
12 J. Lu, H. Liu, S. Deng, M. Zheng, Y. Wang, J.A. Kan, S.H. Tang, X. Zhang, C.H. So and S.G. Mhaisalkar, *Nanoscale,* 2014, **6**, 7619.
13 H. Yoon, M. Choi, T.W. Lim, H. Kwon, K. Ihm, J.K. Kim, S.Y. Cho and J. Son, *Nat. Mater.,* 2016, **15**, 1113.
14 L. Fan, Y. Chen, Q. Liu, S. Chen, L. Zhu, Q. Meng, B. Wang, Q. Zhang, H. Ren and C. Zou, *ACS Appl. Mater. Interf,* 2016, **8**, 32971.
15 Y.Y. Luo, L. Q. Zhu, Y.X. Zhang, S.S. Pan, S.C. Xu, M. Liu and G.H. Li, *J. Appl. Phys.*, 2013, **113**, 183520.
16 M. Borek, F. Qian, V. Nagabushnam and R. K. Singh, *Appl. Phys. Lett.,* 1993, **63**, 3288; S. Lysenko, V. Vikhnin, F. Fernandez, A. Rua and H. Liu, *Phys. Rev. B*, 2007, **75**, 075109.
17 D.H. Kim and H.S. Kwok, *Appl. Phys. Lett.*, 1994, **65**, 3188.
18 L.L. Fan, S. Chen, Y.F. Wu, F.H. Chen, W.S. Chu, X. Chen, C.W. Zou and Z.Y. Wu, *Appl. Phys. Lett.*, 2013, **103,** 131914.
19 A.M. Makarevich, I.I. Sadykov, D.I. Sharovarov, V.A. Amelichev, A.A. Adamenkov, D.M. Tsymbarenko, A.V. Plokhih, M.N. Esaulkov, P.M. Solyankin and A.R. Kaul, *J. Mater. Chem. C*, 2015, **3**, 9197.
20 K. Zhang, M. Tangirala, D. Nminibapiel, W. Cao, V. Pallem, C. Dussarrat and H. Baumgart, *ECS Trans.*, 2013, **50,** 175.
21 C. Cheng, H. Guo, A. Amini, K. Liu, D. Fu, J. Zou and H. Song, *Sci. Rep.*, 2014, **4**, 5456.
22 O. Monfort, T. Roch, L. Satrapinskyy, M. Gregor, T. Plecenik, A. Plecenik, G. Plesch, *Appl. Surf. Sci.*, 2014, **322**, 21.
23 H.-G. Chen, C.-W. Wang and Z.-F. Tu, *Mater. Chem. Phys*., 2014, **144**, 199.
24 H.-G. Chen, C.-W. Wang and Z.-F. Tu, *Mater. Lett.,* 2013, **107**, 276.
25 G. Liu, L. Ma, L.-C. Yin, Y. Liang, J. Tan, H.-M. Cheng, *Joule,* 2018, **2**, 1095.
26 P. Zhang, C. Gao, Y. Wei, C. Dong, C. Jia, Q. Liu and D. Xue, *Appl. Phys. Lett.*, 2014, **105**, 152904.
27 Y.-C. Chieh, C.-C. Yu and F.-H. Lu, *Appl. Phys. Lett.*, 2007, **90**, 032904.
28 Y. Oka, T. Ohtani, N. Yamamoto and T. Takada, *J. Ceram. Soc. Jap.*, 1989, **97**, 1134.
29 C. Leroux, G. Nihoul and G. V. Tendeloo, *Phys. Rev. B: Condens. Matter*, 1998, **57**, 5111.
30 D. Hagrman, J. Zubieta, C.J. Warren, L.M. Meyer, M.M.J. Treacy and R.C. Haushalter, *J. Solid State Chem.*, 1998, **138**, 178.
31 B. Y. Qu, L. Liu, Y. Xie and B.C. Pan, *Phys. Lett. A*, 2011, **375**, 3474.
32 C. Wu, Z. Hu, W. Wang, M. Zhang, J. Yang and Y. Xie, *Chem. Commun.,* 2008, 3891.
33 M. Li, S. Magdassi, Y. Gao and Y. Long, *Small*, 2017, **13**, 1701147.
34 C. Tsang, A. Manthiram, *J. Electrochem. Soc.* 1997, **144**, 520.
35 Z. Khan, B. Senthil Kumar, S.O. Park, S. Park, J. Yang, J.H. Lee, H. Song, Y. Kim, S.K. Kwak and H. Ko, *J. Mater. Chem. A*, 2017, **5**, 2037.
36 S. Lee, I.N. Ivanov, J.K. Keum, H.N. Lee, *Scient. Rep.*, 2016, **6**, 19621.
37 C. Wu, X. Zhang, J. Dai, J. Yang, Z. Wu, S. Wei and Y. Xie, *J. Mater. Chem.*, 2011, **21**, 4509.
38 M.J. Powell, P. Marchand, C.J. Denis, J.C. Bear, J.A. Darr, and I.P. Parkin, *Nanoscale*, 2015, **7**, 18686.
39 S. Zhang, Y. Li, C. Wu, F. Zheng and Y. Xie, *J. Phys. Chem. C,* 2009, **113**, 15058.
40 H. Yin, K. Yu, Z. Zhang, M. Zeng, L. Lou and Z. Zhu, *Electroanal.*, 2011, **23**, 1752.
41 H. Yin, K. Yu, Z. Zhang and Z. Zhu, *Appl. Surf. Scien.,* 2011, **257**, 8840.
42 E. Uchaker, M. Gu, N. Zhou, Y. Li, C. Wang and G. Cao, *Small,* 2013, **9**, 3880.
43 J. Zhang, H. Jin, Z. Chen and J. Li, *Chem. Mater.,* 2015, **27**, 7419.
44 D. Guo, Z. Zhao, J. Li, J. Zhang, R. Zhang, Z. Wang, P. Chen, Y. Zhao, Z. Chen and H. Jin., *Cryst. Growth Des.*, 2017, **17**, 5838.
45 Z. Song, L. Zhang, F. Xia, N. Webster, J. Song, B. Liu, H. Luo and Y. Gao, *Inorg. Chem. Front.*, 2016, **3**, 1035.
46 P. Shvets, O. Dikaya, K. Maksimova and A.Yu. Goikhman, *J. Raman Spectr.*, 2019, **50**, 1226.
47 S.R. Popuri, M. Miclau, A. Artemenko, C. Labrugere, A. Villesuzanne and M. Pollet, *Inorg. Chem.*, 2013, **52**, 4780.
48 Y. Luo, M. Li and G. h. Li, *Chin. J. Chem. Phys.,* 2014, **27**, 471.
49 H.Y. Xu, K.W. Xu, F. Ma and P.K. Chu., *RSC Adv.*, 2018, **8**, 10064.
50 C. Cao, Y. Gao and H. Luo, *J. Phys. Chem. C,* 2008, **112**, 18810.